


Nondissipative Martensitic Phase Transformation after Multimillion Superelastic Cycles

Mostafa Karami^{1,2}, Zeyuan Zhu¹, Ka Hung Chan^{1,3}, Peng Hua¹, Nobumichi Tamura³, and Xian Chen^{1,*}

¹*Department of Mechanical and Aerospace Engineering, The Hong Kong University of Science and Technology, Clear Water Bay, Kowloon, Hong Kong*

²*Department of Materials Science and Engineering, Sharif University of Technology, Tehran, Iran*

³*Advanced Light Source, Lawrence Berkeley National Laboratory, Berkeley, California, USA*

 (Received 10 August 2023; revised 24 October 2023; accepted 22 December 2023; published 7 February 2024)

Superelastic alloys used for stents, biomedical implants, and solid-state cooling devices rely on their reversible stress-induced martensitic transformations. These applications require the alloy to sustain high deformability over millions of cycles without failure. Here, we report an alloy capable of enduring 10×10^7 tensile stress-induced phase transformations while still exhibiting over 2% recoverable elastic strains. After millions of cycles, the alloy is highly reversible with zero stress hysteresis. We show that the major martensite variant is reversible even after multimillions of cycles under tensile loadings with a highly coherent $(1\bar{1}0)_A$ interface. This discovery provides new insights into martensitic transformation, and may guide the development of superelastic alloys for multimillion cycling applications.

DOI: [10.1103/PhysRevLett.132.066101](https://doi.org/10.1103/PhysRevLett.132.066101)

Alloys with reversible solid-solid phase transformations exhibit functionalities such as shape memory effect, superelasticity, caloric cooling, sensing and actuation widely used in smart actuation [1], cardiovascular stents [2,3] and solid-state refrigerators [4,5]. Emerging alloy applications require recoverable strains to withstand millions of stress-induced transformation cycles. Unfortunately, very rare transforming materials meet this requirement. The primary cause of phase reversibility loss during cyclic transformations is lattice mismatch between austenite and martensite. Recoverable strain degrades quickly under cyclic stress-induced transformations. For example, Nitinol, the most popular shape memory alloy, only endures 100 tensile and 1000 compressive cycles [6–8]. Its fatigue life can be improved by microstructure engineering [9,10], but these methods cause local amorphization [10] and lattice distortions [11], significantly increasing the driving force for superelastic strain. For example, the nanocomposite NiTi requires over 1 GPa stress to achieve 2% strain [10].

In recent years, new alloys have been developed to achieve a high fatigue resistance by the phase engineering methods [12–16]. As a result, some superelastic thin films can survive over 10×10^7 stress-induced transformations [13,16], some bulk alloys show extremely small thermal hysteresis [14,17], and some transforming functional ceramics show singular transport properties with a high fatigue life [18–20]. Cofactor conditions (CC) [17] with subconditions CC1-3 [14] are key development criteria. CC1: $\lambda_2 = 1$, where λ_2 is the middle eigenvalue of the stretch tensor $\mathbf{U} \in \mathbb{R}^{3 \times 3}$ [21], significantly affects the thermal hysteresis in phase transforming materials. The thermal hysteresis is minimized at $\lambda_2 = 1$ in many material systems such as TiNi-based [14,17,22,23], CuZn-based

[12,24], and CuAl-based [25–27] alloys and Heusler alloys [28–30]. Experimental results indicate that small deviations from $\lambda_2 = 1$ can lead to significant thermal hysteresis increases for reversible phase transformations. The phase reversibility is believed to be also enhanced as λ_2 approaches 1, as observed in some alloys [12,13,22,24,29]. However, the superelastic alloy CuAl₂₄Mn₉ demonstrates a counterexample [25,31], which exhibits exceptional reversibility over 10 000 cycles of stress-induced transformations despite λ_2 deviating from 1. This suggests that phase reversibility may not solely depend on the $\lambda_2 = 1$ condition, particularly for stress-induced phase transformations. The primary compatibility condition may be sufficient but not necessary to achieve high reversibility during stress-induced transformations. Figure 1 shows the stress hysteresis versus λ_2 for various martensitic alloys. The trend of stress hysteresis is clustered around $\lambda_2 = 1$ but with some scattering. It raises a question whether the $\lambda_2 = 1$ condition still dominates the phase reversibility of stress-induced transformation, especially over long-lasting mechanical cycles.

From a microstructure perspective, the CC1 condition suggests a twinless structure, i.e., the martensite forms as a single lath from the austenite through an atomically sharp interface [32]. Although this microstructure is fully compatible, it limits the morphological flexibility to accommodate nontransforming defects during the phase transformation. For a stress-induced phase transformation, the formation of martensite variants is constrained by the loading orientation. As seen from Fig. 1, the stress hysteresis varies by almost a factor of 2 as the loading orientation changes in Ni₅₀Ti₅₀ ([101] vs [111]) [23] and CuAl₂₄Mn₉ ([001] vs [111]) [25]. It implies that the Gibbs free energy minimizers for the stress-induced phase

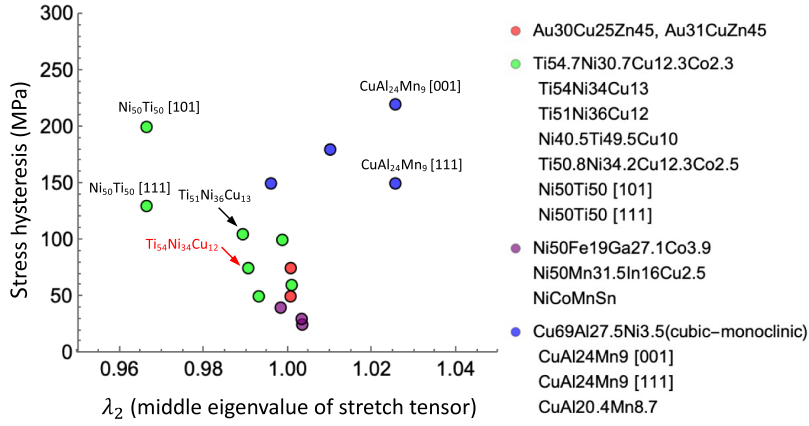


FIG. 1. Relationship between CC1: $\lambda_2 = 1$ and stress hysteresis, for CuZn-based alloys from Refs. [12,24] and this Letter, TiNi-based alloys from Refs. [14,17,22,23], Heusler alloys from Refs. [28–30], and CuAl-based shape memory alloys from Refs. [25–27].

transformation are orientation dependent, more specifically martensite variant dependent. During the axial loading, the formation of martensite variant should maximize the axial strain along the loading direction, and minimize the lateral shear deformation to suppress slips. For martensitic transformation, the martensite variant can be presented by its transformation stretch tensor $\mathbf{U} \in \mathbb{R}^{3 \times 3}$ [21]. The CC2 condition is given by $\mathbf{U}\mathbf{a} \cdot \text{cof}(\mathbf{U}^2 - \mathbf{I})\mathbf{n} = 0$ where the vector $\mathbf{n} \in \mathbb{R}^3$ is the twinning plane normal corresponding to the twinning shear vector $\mathbf{a} \in \mathbb{R}^3$ for the variant \mathbf{U} . Together with CC3: $\text{tr}\mathbf{U}^2 + \det\mathbf{U}^2 - (1/4)|\mathbf{a}|^2|\mathbf{n}|^2 \leq 2$, when the material's lattice parameters satisfy the cofactor conditions for a specific twin system, it can achieve ultimate compatible interfaces between austenite and martensite twin laminates with variable twinning volume fractions [12,14]. The morphology of these compatible twins is flexible, which can accommodate local nontransforming defects and nano or micro cracks. Consequently the reversibility and functional stability over loading cycles can be enhanced.

In this Letter, we explore the superelasticity and functional fatigue resistance of Au₃₁Cu₂₄Zn₄₅ alloy through multimillion stress-induced phase transformations. Alloy development and cofactor conditions calculations are in the Supplemental Material [33–36]. This alloy satisfies the CC1 condition with $\lambda_2 = 1.0067$ (not very close to 1) and CC2 condition with $\mathbf{U}\mathbf{a} \cdot \text{cof}(\mathbf{U}^2 - \mathbf{I})\mathbf{n} = 0.000085$ (very close to 0) for $[1\bar{1}0]$ twofold symmetry axis. For Type I/II twins with $\mathbf{n} = (1\bar{1}0)_A$, CC3 is simultaneously satisfied by direct crystallographic calculation [54]. The martensite phase forms compatible twins rather than a single variant lath. We perform *in situ* uniaxial tensile test on a T-shaped Au₃₁Cu₂₄Zn₄₅ microbeam with width of 3 μm and thickness of 1.5 μm by FemtoTools Nanomechanical Testing System (model FTNMT03, Buchs ZH, Switzerland) under FEI Quanta 250 FEG Scanning Electron Microscope (SEM). We study the phase reversibility and stability under

stress-induced transformations, while observing martensite formation and defect growth. We conduct synchrotron x-ray Laue microdiffraction with energy scans to characterize the loading orientation and the lattice parameters of austenite and martensite near the transformation temperature at Beamline 12.3.2, Advanced Light Source, Lawrence Berkeley National Lab. Figure S2(a) in the Supplemental Material [33] gives the orientation map, from which we determined the loading direction as $\mathbf{t} = [0.09822, 0.48906, 0.8667] \approx [159]$ in terms of the cubic basis. After long cyclic fatigue tests, we analyze phase interfaces, twins, and nontransforming defects at nano to atomic scales to uncover million-cycle reversibility mechanisms.

Figure 2 shows the transformability and reversibility of the specimen under tensile stress-induced transformation up to 10^6 cycles. The fatigue tests were conducted at a high loading frequency of 10 Hz for the first 10^6 cycles, and at a larger loading frequency of 15 Hz up to 10^7 cycles. To minimize the effect of the thermal drift during long cycling experiments, we paused the test and recalibrated the thermal drift every 100 000 cycles for 10 Hz and 15 Hz loading rate experiments. During the first 100 000 tensile cycles, the transforming material is fully reversible. The stress-strain responses are almost identical without any nominal residual strains in Fig. 2(a). The Supplemental Movie S1 shows a full superelastic cycle of the specimen under tensile stress-induced transformation. Based on crystallographic theory of martensite [21,24,25,31], we calculated the compatible twin laminates, listed in Table S1 [33], corresponding to the axial tensile strain, $\epsilon_{\text{cal}} = 0.037$, which agrees with the superelastic strain, $\epsilon_t = 0.034$, measured as the plateau strain shown in Fig. 2(a). The transformation stress is determined as 300 MPa with about 80 MPa stress hysteresis corresponding to 4.5% total recoverable strains without degradation up to 200 000 transformation cycles.

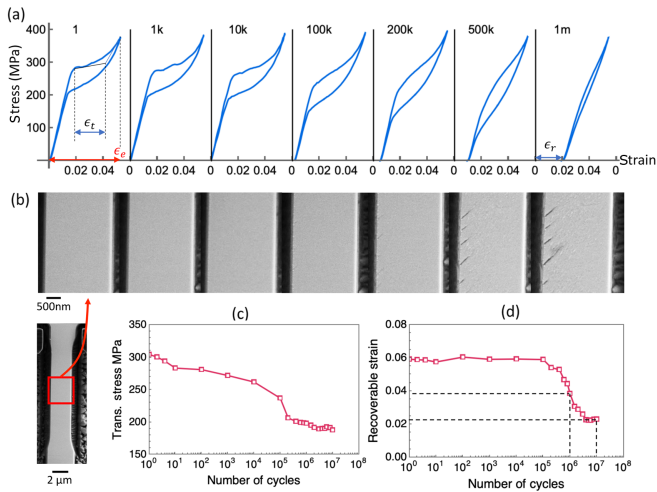


FIG. 2. The superelasticity and the growth of the nanocracks in $\text{Au}_{31}\text{Cu}_{24}\text{Zn}_{45}$ up to 10^6 tensile stress-induced phase transformations. (a) Stress-strain behaviors of the microbeam at the 1st, 1000th, 10 000th, 100 000th, 200 000th, 500 000th and 10^6 th mechanical cycles, corresponding to (b) the lateral surface microstructure at the maximum tensile stretch. The functional degradation of the specimen is plotted for (c) transformation stress and (d) recoverable strain (i.e., superelastic strain) over number of cycles.

As seen in Fig. 2(b), the lateral surface is clean except for several nanoscale defects on the left side of the specimen, nucleated from 100 000 cycles. In subsequent tensile

cycles, the specimen is loaded up to 400 MPa to complete the transformation from austenite to martensite. After 200 000 cycles, the residual strain accumulates with increasing cycle number, while the superelastic strain and stress hysteresis are reduced. The superelastic behavior becomes less noticeable after 500 000 cycles with almost 90% decrease in stress hysteresis. Beyond this stage, we use the recoverable strain to represent the superelastic functionality. After 10^6 cycles, the growth of nanocracks results in an accumulation of approximately 0.02 residual strain (denoted as ϵ_r). Despite this, the sample is still able to maintain an almost 0.04 total recoverable strain (i.e., elastic strain ϵ_e) throughout the loading and unloading process. Additionally, there is a significant reduction in stress hysteresis compared to the first cycle. The Supplemental Movie S2 shows 40 consecutive cycles of tensile stress-induced transformations after 10^6 cycles. The specimen is still reversible and deformable with an output of 4% recoverable strain, while no conspicuous structural defects were observed on the lateral surface of the specimen.

Beyond 10^6 cycles, we continued the mechanical tests on the $\text{Au}_{31}\text{Cu}_{24}\text{Zn}_{45}$ microbeam to obtain the stress-strain responses associated with the growth of the nanocracks in Figs. 3(a) and 3(b). From the 2×10^6 cycle, the stress hysteresis became zero and the propagation of nanocracks in the specimen stopped. Figures 2(c) and 2(d) show that the stress-strain behavior converges, and over 0.02 recoverable strain was achieved and stabilized beyond million

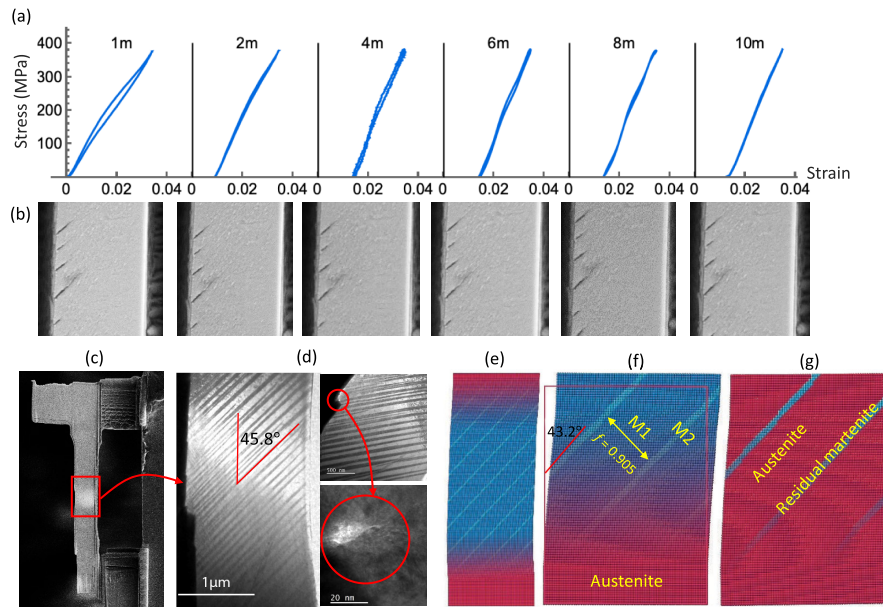


FIG. 3. The transformability and reversibility of the $\text{Au}_{31}\text{Cu}_{24}\text{Zn}_{45}$ microbeam beyond the 10^6 mechanical cycles. (a) Stress-strain responses under the tensile loading at the 10^6 , 2×10^6 , 4×10^6 , 6×10^6 , 8×10^6 , and 10×10^6 cycles, associated with (b) the grown nanocracks on the lateral surface. (c) The TEM foil fabricated for the (d) transmission electron microscope observation of the microbeam after 10×10^6 mechanical cycles. (e) Prediction of the formation of the compatible twin laminates with volume fraction of 0.905. (f) Morphological configuration of the compatible interfaces among austenite, major variant M1 and minor variant M2, compared to (g) the compatible interfaces between austenite and residual martensite M2.

cycles. Strictly speaking, the mechanical behavior at this stage is not conventionally superelastic. The transformability of the tensile specimen remains quite promising with a total one-way work of $\sim 4 \text{ MJ/m}^3$, estimated as the bulk elastic energy gained upon loading. As a comparison, the one-way work under tensile stress in NiTi (bulk) is 10 MJ/m^3 , but it degrades to 5 MJ/m^3 after only 100 cycles [6]. In magnetic shape memory alloys such as Ni_2MnGa , the one-way work in the first cycle is about 3 MJ/m^3 [55]. This suggests that the compatible alloy is still functional even after 10×10^7 superelastic cycles. From SEM images of Fig. 3(b), the structural defects were stabilized as the same microstructure was captured at 2×10^6 , 4×10^6 , 6×10^6 , 8×10^6 , and 10×10^6 cycles. The Supplemental Movie S3 shows 40 consecutive stress-induced transformations after 10×10^7 cycles. The post-cycled microbeam does not show nominal strain hardening or conventional slips even after numerous deformation cycles. The combination of large transformability and exceptional resilience provide a great potential for engineering applications in biomedical industries and energy science.

The postcycled microbeam was prepared for transmission electron microscope (TEM) experiments to study the mechanism responsible for the reversibility beyond 10^6 cycles. A tiny surface step was observed on the left side where the nanocracks nucleate. It suggests that the plasticity may have initialized during the cycling history. The open crack propagated along the laminates, then was closed after traveling a 20 nm distance. Signs of crossing slip lines were not observed in this specimen. Instead, Figs. 3(c) and 3(d) suggest the presence of residual martensite phase. Based on the compatibility theory [14,21], we calculate the compatible twin laminates shown in Figs. 3(e) and 3(f). The details of the calculation are given in the Supplemental Material [33]. The calculated compatible twins consist of a major martensite variant M1 (dark blue) and a minor variant M2 (light blue) with a volume fraction 0.905 given in Fig. 3(f). The transformation strain given by the minor variant of martensite is calculated as $\epsilon_{M2} = 0.0186$. Considering that about half of the region is occupied by the residual martensite [Fig. 3(d)], the minor variant M2 contributes to ~ 0.01 residual strain in the specimen. The transformation strain of the major variant M1 is $\epsilon_{M1} = 0.039$, corresponding to ~ 0.02 recoverable strain in the specimen. This calculation well agrees with the *in situ* nanomechanics experiment in Fig. 3(a). It suggests that the minor variant is pinned while the major variant is still reversible after 10×10^7 stress-induced transformation cycles.

In addition, we calculated the postcycled microstructure of the austenite and residual martensite (i.e., M2 minor variant) in Fig. 3(g). The calculated deformation field and the interfaces agree with the experimental observation in Fig. 3(d). In our model, there is an elastic transition layer

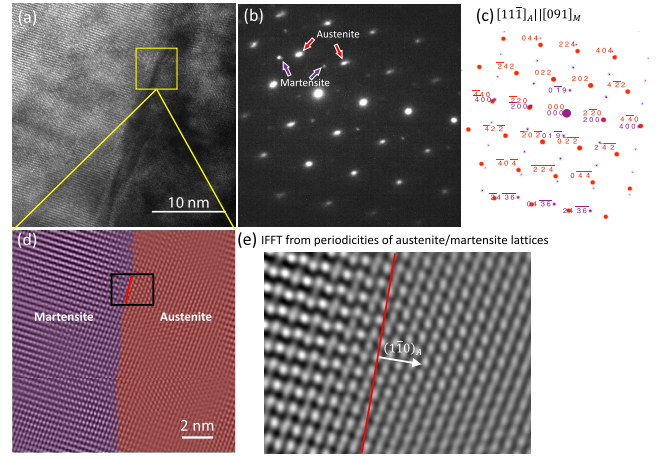


FIG. 4. (a) High resolution TEM image of the postdeformed specimen near the interface between laminates. (b) The diffraction patterns from the lattices on both sides (c) indexed by austenite (red) $Fm\bar{3}m$ symmetry, and martensite (purple) $P2_1$ symmetry. (d) Resolved interface morphology with an enlarged reconstructed inverse Fourier transform of the austenite and martensite lattices. (e) Lattice periodicities of austenite and martensite with an interface aligned with the twinning plane $(1\bar{1}0)_A$.

between austenite and the twinned martensite but the lattice distortion is very small, as the CC2 condition of this twin pair is closely satisfied, i.e., $CC2 = 0.00085$ for both type I and II twins with the twofold axis $[1\bar{1}0]$. The numerical details are given in Table S1 in Supplemental Material [33]. The vanishing of CC2 suggests a highly coherent interface in deformed configuration between austenite and martensite through normals of type I and II twinning planes, i.e., either \mathbf{n} or \mathbf{Ua} . The calculated microstructure confirms such a high coherency at the austenite-M2 interface. To further verify the interface, we conducted the high resolution TEM study [Fig. 4(a)]. The selected area diffraction patterns of the regions reveal that the two phases are austenite and a variant of martensite, as seen in Figs. 4(b) and 4(c). The interface closely aligned with the $(1\bar{1}0)_A$ plane, corresponding to the $(100)_M$ plane. The phase contrast images from the selected subregion of Fig. 4(a) were reconstructed by fast Fourier transform and inverse Fourier transform [Fig. 4(e)]. We can clearly distinguish two periodicities from one side (austenite) to the other (martensite), and they are not mirror-symmetry related.

In addition, the CC2 condition ensures the flexibility of twin laminates morphology, the nontransforming defects can be accommodated during the stress-induced transformation. In both pre and postcycled specimens, the dislocation density is very low, verified by the TEM observations in Figs. 3(c), 3(d), 4(a), and S3 in the Supplemental Material. The highly coherent interfaces satisfying the CC2 condition stabilize the nanocracks and other nontransforming defects. Beyond sufficiently many deformation cycles, the phase transformation has

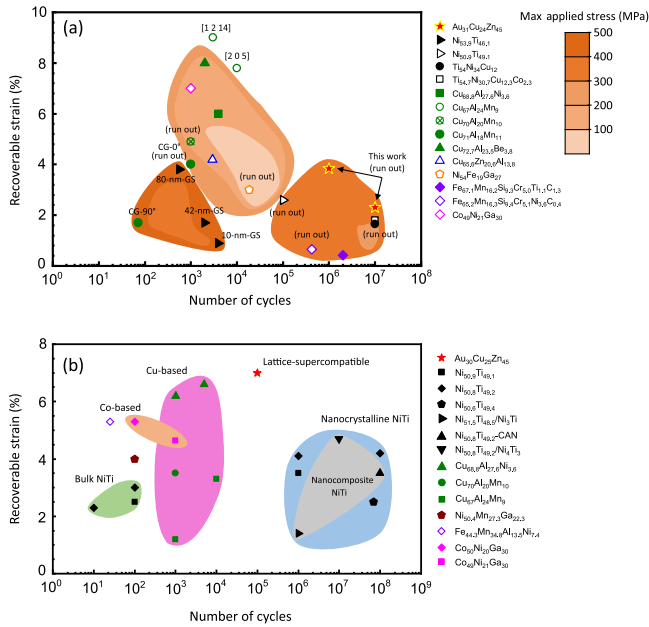


FIG. 5. Comparison of the cycle-number dependent recoverable strain under (a) tension and (b) compression among common superelastic alloys such as NiTi-based alloys [7,8,10,13,37–43], CuAl- and CuZn-based alloys [8,25,31,44–48], FeNi-based alloys [49–53], AuCuZn alloys [24]. In (a), maximum stress contours during tensile cycling are overlaid. In (a) and (b), CG-0° and CG-90° represent columnar-grained samples oriented in 0° and 90° to the solidification direction, GS denotes grain size, and CAN means crystalline-amorphous nanocomposite. Alloy details and references are in Supplemental Tables S2 and S3.

become nondissipative. The observed residual strain is primarily attributed to the minor martensite variant. The rest austenite region is still reversible because of the highly coherent and compatible interfaces between austenite and martensite. No further degradation will occur beyond this stage.

In conclusion, we analyzed recoverable strains in various transforming alloys under stress-induced transformations (Fig. 5). Fatigue resistance of these alloys is lower under tension than compression, but recoverable strains are higher. The tensile loading is an effective actuation force but is demanding. Figure 5(a) shows the tensile strains of most superelastic alloys are around 4%, which survive 1000 ~ 100 000 transformation cycles at 200–300 MPa stress. The compatible Au₃₁Cu₂₄Zn₄₅ alloy exhibits 4% recoverable strain after 10⁶ cycles, and 2% beyond 10 × 10⁶ cycles. This alloy was tested at a miniature size, in which the dislocations and nontransforming defects can easily slip across the specimen. But they are suppressed by coherent austenite-martensite interfaces. Comparing fatigue resistance under compression in Fig. 5(b), the compatible Au₃₀Cu₂₄Zn₄₅ demonstrates an exceptional 7% recoverable strain after 100 000 transformation cycles without functional degradation. It suggests that microstructure compatibility significantly enhances the

reversibility of stress-induced phase transformation without strain hardening. Particularly, satisfying the cofactor condition CC2 enables compatible austenite and twinned martensite, minimizing the lattice distortion in the elastic transition layer, and stabilizing the nontransforming defect during deformation cycles. Beyond sufficient number of cycles, the phase transformation becomes nondissipative. The nondissipative nature ensures the exceptional resilience and superelastic performance, providing a basis for superelastic material’s development in biomedical and energy applications.

M. K., Z. Z., K. H. C., and X. C. thank the financial support under GRF Grants No. 16203021 and No. 16204022 by Research Grants Council, Hong Kong. M. K., Z. Z., P. H., and X. C. acknowledge the financial support under CRF Grant No. C6016-20G-C by Research Grants Council, Hong Kong. This research used Beamline 12.3.2, a resource of the Advanced Light Source, which is a DOE Office of Science User Facility under Award No. DE-AC02-05CH11231.

*Corresponding author: xianchen@ust.hk

- [1] K. Bhattacharya and R. D. James, The material is the machine, *Science* **307**, 53 (2005).
- [2] T. Yoneyama and S. Miyazaki, *Shape Memory Alloys for Biomedical Applications* (Elsevier, New York, 2008).
- [3] A. Biesiekierski, J. Wang, M. A. H. Gepreel, and C. Wen, A new look at biomedical Ti-based shape memory alloys, *Acta Biomater.* **8**, 1661 (2012).
- [4] E. Bonnot, R. Romero, L. Mañosa, E. Vives, and A. Planes, Elastocaloric effect associated with the martensitic transition in shape-memory alloys, *Phys. Rev. Lett.* **100**, 125901 (2008).
- [5] L. Mañosa and A. Planes, Materials with giant mechano-caloric effects: Cooling by strength, *Adv. Mater.* **29**, 1603607 (2017).
- [6] S. Miyazaki, T. Imai, Y. Igo, and K. Otsuka, Effect of cyclic deformation on the pseudoelasticity characteristics of Ti – Ni alloys, *Metall. Trans. A* **17**, 115 (1986).
- [7] K. Otsuka and X. Ren, Physical metallurgy of Ti – Ni-based shape memory alloys, *Prog. Mater. Sci.* **50**, 511 (2005).
- [8] M. Karami and X. Chen, Nanomechanics of shape memory alloys, *Mater. Today Adv.* **10**, 100141 (2021).
- [9] P. Hua, K. Chu, F. Ren, and Q. Sun, Cyclic phase transformation behavior of nanocrystalline NiTi at microscale, *Acta Mater.* **185**, 507 (2020).
- [10] P. Hua, M. Xia, Y. Onuki, and Q. Sun, Nanocomposite NiTi shape memory alloy with high strength and fatigue resistance, *Nat. Nanotechnol.* **16**, 409 (2021).
- [11] H. Chen, Y.-D. Wang, Z. Nie, R. Li, D. Cong, W. Liu, F. Ye, Y. Liu, P. Cao, F. Tian, X. Shen, R. Yu, L. Vitos, M. Zhang, S. Li, Z. Xiaoyu, H. Zheng, J. F. Mitchell, and Y. Ren, Unprecedented non-hysteretic superelasticity of [001]-oriented nicofega single crystals, *Nat. Mater.* **19**, 712 (2020).

- [12] Y. Song, X. Chen, V. Dabade, T. W. Shield, and R. D. James, Enhanced reversibility and unusual microstructure of a phase-transforming material, *Nature (London)* **502**, 85 (2013).
- [13] C. Chluba, W. Ge, R. Lima de Miranda, J. Strobel, L. Kienle, E. Quandt, and M. Wuttig, Ultralow-fatigue shape memory alloy films, *Science* **348**, 1004 (2015).
- [14] X. Chen, V. Srivastava, V. Dabade, and R. D. James, Study of the cofactor conditions: Conditions of supercompatibility between phases, *J. Mech. Phys. Solids* **61**, 2566 (2013).
- [15] J. Cui, Y. S. Chu, O. O. Famodu, Y. Furuya, J. Hattrick-Simpers, R. D. James, A. Ludwig, S. Thienhaus, M. Wuttig, Z. Zhang *et al.*, Combinatorial search of thermoelastic shape-memory alloys with extremely small hysteresis width, *Nat. Mater.* **5**, 286 (2006).
- [16] H. Gu, L. Bumke, C. Chluba, E. Quandt, and R. D. James, Phase engineering and supercompatibility of shape memory alloys, *Mater. Today* **21**, 265 (2018).
- [17] Z. Zhang, R. D. James, and S. Müller, Energy barriers and hysteresis in martensitic phase transformations, *Acta Mater.* **57**, 4332 (2009).
- [18] J. Jetter, H. Gu, H. Zhang, M. Wuttig, X. Chen, J. R. Greer, R. D. James, and E. Quandt, Tuning crystallographic compatibility to enhance shape memory in ceramics, *Phys. Rev. Mater.* **3**, 093603 (2019).
- [19] Y. Liang, S. Lee, H. Yu, H. Zhang, Y. Liang, P. Y. Zavalij, X. Chen, R. D. James, L. A. Bendersky, A. V. Davydov *et al.*, Tuning the hysteresis of a metal-insulator transition via lattice compatibility, *Nat. Commun.* **11**, 1 (2020).
- [20] C. Zhang, Z. Zeng, Z. Zhu, N. Tamura, and X. Chen, Energy conversion from heat to electricity by highly reversible phase-transforming ferroelectrics, *Phys. Rev. Appl.* **16**, 024064 (2021).
- [21] J. M. Ball and R. D. James, Fine phase mixtures as minimizers of energy, *Arch. Ration. Mech. Anal.* **100**, 13 (1987).
- [22] R. Zarnetta, R. Takahashi, M. L. Young, A. Savan, Y. Furuya, S. Thienhaus, B. Maaß, M. Rahim, J. Frenzel, H. Brunken *et al.*, Identification of quaternary shape memory alloys with near-zero thermal hysteresis and unprecedented functional stability, *Adv. Funct. Mater.* **20**, 1917 (2010).
- [23] R. Manjeri, S. Qiu, N. Mara, A. Misra, and R. Vaidyanathan, Superelastic response of [111] and [101] oriented NiTi micropillars, *J. Appl. Phys.* **108** (2010).
- [24] X. Ni, J. R. Greer, K. Bhattacharya, R. D. James, and X. Chen, Exceptional resilience of small-scale $\text{Au}_{30}\text{Cu}_{25}\text{Zn}_{45}$ under cyclic stress-induced phase transformation, *Nano Lett.* **16**, 7621 (2016).
- [25] M. Karami, Z. Zhu, Z. Zeng, N. Tamura, Y. Yang, and X. Chen, Two-tier compatibility of superelastic bicrystal micropillar at grain boundary, *Nano Lett.* **20**, 8332 (2020).
- [26] N. Zarubova and V. Novák, Phase stability of CuAlMn shape memory alloys, *Mater. Sci. Eng. A* **378**, 216 (2004).
- [27] R. D. James and Z. Zhang, A way to search for multiferroic materials with “unlikely” combinations of physical properties, in *Magnetism and Structure in Functional Materials*, edited by A. Planes, L. Mañosa, and A. Saxena (Springer, Berlin, Heidelberg, 2005), pp. 159–175.
- [28] V. Srivastava, X. Chen, and R. D. James, Hysteresis and unusual magnetic properties in the singular Heusler alloy $\text{Ni}_{45}\text{Co}_5\text{Mn}_{40}\text{Sn}_{10}$, *Appl. Phys. Lett.* **97**, 014101 (2010).
- [29] D. Zhao, J. Liu, X. Chen, W. Sun, Y. Li, M. Zhang, Y. Shao, H. Zhang, and A. Yan, Giant caloric effect of low-hysteresis metamagnetic shape memory alloys with exceptional cyclic functionality, *Acta Mater.* **133**, 217 (2017).
- [30] Y. Li, D. Zhao, J. Liu, S. Qian, Z. Li, W. Gan, and X. Chen, Energy-efficient elastocaloric cooling by flexibly and reversibly transferring interface in magnetic shape-memory alloys, *ACS Appl. Mater. Interfaces* **10**, 25438 (2018).
- [31] M. Karami, K. Chu, Z. Zhu, Z. Wang, Q. Sun, M. Huang, and X. Chen, Orientation-dependent superelasticity and fatigue of CuAlMn alloy under *in situ* micromechanical tensile characterization, *J. Mech. Phys. Solids* **160**, 104787 (2022).
- [32] R. Delville, S. Kasinathan, Z. Zhang, J. V. Humbeeck, R. D. James, and D. Schryvers, Transmission electron microscopy study of phase compatibility in low hysteresis shape memory alloys, *Philos. Mag.* **90**, 177 (2010).
- [33] See Supplemental Material, which includes Refs. [8–10,13,14,24,25,31,34–53], at <http://link.aps.org/supplemental/10.1103/PhysRevLett.132.066101> for materials and methods, compatibility conditions of austenite-martensite interfaces, algorithm for austenite-martensite interfaces, Fig. S1–S4, Tables S1–S3, captions of Movies S1–S3.
- [34] X. Chen, N. Tamura, A. MacDowell, and R. D. James, In-situ characterization of highly reversible phase transformation by synchrotron x-ray laue microdiffraction, *Appl. Phys. Lett.* **108**, 211902 (2016).
- [35] J. M. Ball and R. D. James, Proposed experimental tests of a theory of fine microstructure and the two-well problem, *Phil. Trans. R. Soc. A* **338**, 389 (1992).
- [36] Y. Song, N. Tamura, C. Zhang, M. Karami, and X. Chen, Data-driven approach for synchrotron x-ray laue microdiffraction scan analysis, *Acta Crystallogr. Sect. A* **75**, 876 (2019).
- [37] H. Yin, Y. He, Z. Moumni, and Q. Sun, Effects of grain size on tensile fatigue life of nanostructured NiTi shape memory alloy, *Int. J. Fatigue* **88**, 166 (2016).
- [38] J. Tušek, A. Žerovnik, M. Čebren, M. Brojan, B. Žužek, K. Engelbrecht, and A. Cadelli, Elastocaloric effect vs fatigue life: Exploring the durability limits of Ni – Ti plates under pre-strain conditions for elastocaloric cooling, *Acta Mater.* **150**, 295 (2018).
- [39] H. Lin, P. Hua, K. Huang, Q. Li, and Q. Sun, Grain boundary and dislocation strengthening of nanocrystalline NiTi for stable elastocaloric cooling, *Scr. Mater.* **226**, 115227 (2023).
- [40] P. Hua, H. Lin, and Q. Sun, Ultrahigh cycle fatigue deformation of polycrystalline NiTi micropillars, *Scr. Mater.* **203**, 114108 (2021).
- [41] J. Chen, K. Zhang, Q. Kan, H. Yin, and Q. Sun, Ultra-high fatigue life of NiTi cylinders for compression-based elastocaloric cooling, *Appl. Phys. Lett.* **115**, 093902 (2019).
- [42] H. Hou, E. Simsek, T. Ma, N. S. Johnson, S. Qian, C. Cissé, D. Stasak, N. Al Hasan, L. Zhou, Y. Hwang *et al.*, Fatigue-resistant high-performance elastocaloric materials made by additive manufacturing, *Science* **366**, 1116 (2019).
- [43] F. Xiao, K. Chu, Z. Li, R. Hou, Y. Gao, Q. Sun, and X. Jin, Improved functional fatigue resistance of single crystalline

- NiTi micropillars with uniformly oriented Ti_3Ni_4 precipitates, *Int. J. Plast.* **160**, 103480 (2023).
- [44] J. Liu, H. Huang, and J. Xie, Superelastic anisotropy characteristics of columnar-grained Cu – Al – Mn shape memory alloys and its potential applications, *Mater. Des.* **85**, 211 (2015).
- [45] C. Qiu and S. Zhu, Characterization of cyclic properties of superelastic monocrystalline Cu – Al – Be SMA wires for seismic applications, *Constr. Build. Mater.* **72**, 219 (2014).
- [46] S. M. Ueland and C. A. Schuh, Superelasticity and fatigue in oligocrystalline shape memory alloy microwires, *Acta Mater.* **60**, 282 (2012).
- [47] J. F. Gómez-Cortés, M. L. Nó, I. Ruíz-Larrea, T. Brezowski, A. López-Echarri, C. A. Schuh, and J. M. San Juan, Ultrahigh superelastic damping at the nano-scale: A robust phenomenon to improve smart MEMS devices, *Acta Mater.* **166**, 346 (2019).
- [48] J. San Juan, J. Gómez-Cortés, G. López, C. Jiao, and M. Nó, Long-term superelastic cycling at nano-scale in Cu – Al – Ni shape memory alloy micropillars, *Appl. Phys. Lett.* **104**, 011901 (2014).
- [49] C. Efstathiou, H. Sehitoglu, P. Kurath, S. Foletti, and P. Davoli, Fatigue response of NiFeGa single crystals, *Scr. Mater.* **57**, 409 (2007).
- [50] K. N. Hong, Y. M. Yeon, W. B. Shim, and S. W. Ji, Fatigue characteristics of Fe-based shape-memory alloys, *Appl. Sci.* **10**, 5812 (2020).
- [51] P. Krooß, T. Niendorf, P. Kadletz, C. Somsen, M. Gutmann, Y. Chumlyakov, W. W. Schmahl, G. Eggeler, and H. Maier, Functional fatigue and tension–compression asymmetry in [001]-oriented $\text{Co}_{49}\text{Ni}_{21}\text{Ga}_{30}$ high-temperature shape memory alloy single crystals, *Shape Mem. Superelasticity* **1**, 6 (2015).
- [52] L. Wei, X. Zhang, J. Liu, and L. Geng, Orientation dependent cyclic stability of the elastocaloric effect in textured Ni – Mn – Ga alloys, *AIP Adv.* **8**, 055312 (2018).
- [53] A. Shen, D. Zhao, W. Sun, J. Liu, and C. Li, Elastocaloric effect in a $\text{Co}_{50}\text{Ni}_{20}\text{Ga}_{30}$ single crystal, *Scr. Mater.* **127**, 1 (2017).
- [54] M. Chapman, M. De Graef, R. D. James, and X. Chen, Quantitative analysis of compatible microstructure by electron backscatter diffraction, *Phil. Trans. R. Soc. A* **379**, 20200112 (2021).
- [55] I. Karaman, H. E. Karaca, B. Basaran, D. C. Lagoudas, Y. I. Chumlyakov, and H. J. Maier, Stress-assisted reversible magnetic field-induced phase transformation in Ni_2MnGa magnetic shape memory alloys, *Scr. Mater.* **55**, 403 (2006).